NANO LETTERS
Letter
Cite This: Nano Lett. 2019, 19, 7021−7027
pubs.acs.org/NanoLett

Engineering Electron−Phonon Coupling of Quantum Defects to a Semiconfocal Acoustic Resonator

Huiyao Chen,[†] Noah F. Opondo,[‡] Boyang Jiang,[‡] Evan R. MacQuarrie,[†] Raphaël S. Daveau,[†] Sunil A. Bhave,[‡] and Gregory D. Fuchs*[,†,§]

[†]Cornell University, Ithaca, New York 14853, United States
[‡]Purdue University, West Lafayette, Indiana 47907, United States
[§]Kavli Institute at Cornell for Nanoscale Science, Cornell University, Ithaca, New York 14853, United States

Supporting Information

ABSTRACT: Diamond-based microelectromechanical systems (MEMS) enable direct coupling between the quantum states of nitrogen-vacancy (NV) centers and the phonon modes of a mechanical resonator. One example, a diamond high-overtone bulk acoustic resonator (HBAR), features an integrated piezoelectric transducer and supports high-quality factor resonance modes into the gigahertz frequency range. The acoustic modes allow mechanical manipulation of deeply embedded NV centers with long spin and orbital coherence times. Unfortunately, the spin-phonon coupling rate is limited by the large resonator size, >100 μm, and thus strongly coupled NV electron−phonon interactions remain out of reach in current diamond BAR devices. Here, we report the design and fabrication of a semiconfocal HBAR (SCHBAR) device on diamond (silicon carbide) with $f \times Q > 10^{12}$ ($>10^{13}$). The semiconfocal geometry confines the phonon mode laterally below 10 μm. This drastic reduction in modal volume enhances defect center coupling to a mechanical mode by 1000 times compared to prior HBAR devices. For the native NV centers inside the diamond device, we demonstrate mechanically driven spin transitions and show a high strain-driving efficiency with a Rabi frequency of $(2\pi)2.19(14)$ MHz/V_p, which is comparable to a typical microwave antenna at the same microwave power, making SCHBAR a power-efficient device useful for fast spin control, dressed state coherence protection, and quantum circuit integration.

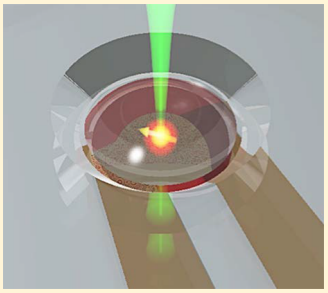

KEYWORDS: *Nitrogen-vacancy center, diamond, silicon carbide, MEMS, bulk acoustic resonator*

Defect-based qubits are attractive platforms for solid state quantum technologies.[1] The leading examples are the nitrogen-vacancy (NV)[2] center and the silicon-vacancy (SiV)[3] center in diamond, and the divacancy center[4] and the silicon vacancy center (V_{Si})[5] in silicon carbide (SiC). Hybrid quantum systems based on these defect qubits are particularly interesting because they interface the qubit spin to photons or phonons and enable unconventional modalities of quantum enhanced sensing[6] and spin state control.[7] Although solid state spin-photon entanglement has been demonstrated in recent years[8] and has been used to build quantum networks,[9] defect-based spin-mechanical systems have yet to operate at the single phonon quantum level because they are limited by weak single electron−phonon coupling, g, in existing devices. Considering $g \propto \sqrt{1/V}$, where V is the modal volume, one approach to strengthening the coupling is to engineer small mode volume mechanical resonators with high quality factors, which calls for challenging experiments that build stepping stones toward a strongly coupled defect spin-phonon system.

Enhancement of g through resonator engineering also benefits more classical applications of the resonator in which mechanical driving is used to improve qubit performance. For example, coherent phonon driving of qubit states yield extended coherence time,[10,11] which is a considerable resource for a range of quantum applications including sensing. More explicitly, the improvement in coherence time is set by the total phonon coupling strength $\sqrt{N_p}g$, which is classically evaluated as the product of resonator strain and strain susceptibility of the defect spin, $\sqrt{N_p}g = \epsilon d = \sqrt{\frac{2U}{EV}}d$, where N_p is the coherent phonon population, U is the mechanical energy stored in the resonator, and E is the Young's modulus of the resonator material.

Existing defect-based spin-mechanical systems can be classified into two categories: (1) microbeam resonator systems[12−14] and (2) microelectromechanical systems (MEMS)[7,15−17] with integrated thin-film piezoelectric transducers. Although the first category minimizes the resonator fabrication to a single material, that is, diamond, SiC, and so forth, high-frequency bulk mode microbeam resonators (>1 GHz) often require optomechanical coupling[13,14] to efficiently excite and detect the resonator state. The latter category includes surface acoustic wave (SAW) and bulk acoustic wave (BAW) devices. These resonator types can be excited and

Received: June 14, 2019
Revised: August 28, 2019
Published: September 9, 2019

DOI: 10.1021/acs.nanolett.9b02430
Nano Lett. 2019, 19, 7021−7027

characterized electrically at gigahertz frequencies, and they enable both quantum circuit integration[18,19] and direct quantum control of embedded defect qubits. At higher frequency (>2 GHz), although SAW devices start to show progressively higher losses, BAW resonators maintain a high quality factor.[20] Additionally, the BAW resonator can couple to defect centers that lie deep inside the device, making them less susceptible to deleterious surface effects and thus they can possess long spin and orbital coherence times.

In an effort to improve the power efficiency of spin-mechanical devices with enhanced coupling between quantum defects and a resonator mode, here we report the design, fabrication, and performance of a new type of diamond (and SiC) BAW device, the semiconfocal high-overtone bulk acoustic resonator (SCHBAR). While the confocal geometry has been demonstrated recently in both SAW[17,21,22] and macroscale BAW devices,[23,24] here we apply the concept to a microscale BAW resonator. The device features a microscale phonon mode volume and integrated atomic-scale quantum defects. Electrical measurements show that the frequency-quality factor product is $f \times Q > 10^{12}$ ($>10^{13}$) for diamond (SiC) SCHBAR devices operating with a ∼3 GHz phonon mode. In a diamond SCHBAR device, we use the native NV centers to characterize the ac strain performance of the acoustic resonator. We mechanically drive NV center ground-state spin Rabi oscillations at a rate $(2\pi)2.19(14)$ MHz/V_p, corresponding to a mechanical strain $1.59(14) \times 10^{-4}$ V_p^{-1}, indicating high power-to-strain conversion efficiency. Applications of this device include the fast quantum control of defect spins in the double-quantum basis, study of spin dynamics in the strong-mechanical-driving regime, and quantum control of resonator states using dense defect spin ensembles.

BAW devices have been widely used in the microelectronics industry for RF filtering and other wireless applications.[25] The transducer of most BAW devices consists of a piezoelectric thin film sandwiched between two electrodes in a released structure or solidly mounted on a planar substrate. The two planar boundaries of the device form a cavity for the bulk acoustic wave. To achieve a high quality factor, a high degree of parallelism for the two planar boundaries is stringently required to suppresses the acoustic diffraction loss.[26] Even with perfectly parallel boundaries, a planar cavity lacks lateral confinement.[27] A partial solution is to make large area transducer to spatially limit the diffraction loss, however, this also constrains the size scale of a standard BAW device to be larger than 100 μm.

In analogy to a confocal or semiconfocal optical cavity, an acoustic cavity with curved boundaries that match the wavefront of the acoustic wave can overcome diffraction loss and provide stable mode confinement. In the far field, the cavity stability criterion suggests that the best confinement is obtained in a confocal geometry or a semiconfocal geometry for a planar convex boundary condition. In this work, we choose to work with diamond and SiC substrates because they possess excellent mechanical properties and their crystal lattices host quantum defects. We design the microresonator for a 10 and a 20 μm thick device.

As illustrated in Figure 1a, the device has a planar−convex structure. We design one side of the resonator with a curved surface, enabling it to confine three-dimensional phonon modes with characteristic dimensions of 10 μm. The radius of curvature of the curved surface is twice the thickness of the substrate in a semiconfocal geometry, giving rise to the device

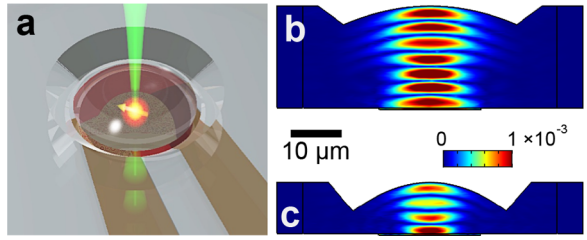

Figure 1. (a) Concept image of the semiconfocal HBAR device design. Solid state defect spins (orange arrow) such as from diamond NV centers are accommodated in the depth of the substrate. They can be addressed optically (laser), magnetically (microwave), and mechanically (acoustics). Brown-colored leads represent the transducer electrodes. The ruby-colored layer is a 500 nm piezoelectric ZnO thin film. (b,c) Strain profiles of the diamond devices simulated by COMSOL for a 3 GHz mode with a 1 V_p voltage driving source. The 20 and 10 μm thick devices have a parabolic curved solid immersion lens with radius of curvature 40 and 20 μm respectively, providing both acoustic confinement and optical refraction suppression.

name, SCHBAR. Compared to a planar cavity, the curved surface eliminates the requirement of boundary parallelism and, in principle, yields higher mechanical quality factors. Optically, the curved surface also acts as a solid immersion lens (SIL). It reduces substrate refraction and thus enhances light extraction from the defects inside the resonator.[28] The defects are microns below the surface and thus are well-protected from fabrication damage and surface effects. On the planar side of the device, we fabricate an integrated piezoelectric transducer and a microwave antenna that is aligned with the center of the resonator, allowing for acoustic and magnetic driving, respectively. The radius of the transducer has been designed to mode-match the waist of the confined acoustic wave, and the thickness of piezoelectric ZnO film is controlled to target a 3 GHz resonance mode which allows stable confinement.

We simulate the mechanical performance of the device using COMSOL. Figure 1b,c shows the strain profile of an ∼3 GHz acoustic mode for a 20 and a 10 μm device with a driving voltage amplitude at V_p = 1 V. The simulation results show stable confinement of the acoustic wave and a peak strain around $5-10 \times 10^{-4}$ V_p^{-1}.

We fabricated SCHBAR devices from both diamond and 4H-SiC substrates.[29] For simplicity, here we restrict the process flow description to diamond, as presented in Figure 2. We start from a 50 μm thick, double-side polished single crystal diamond plate (nitrogen concentration <1 ppm). In the first step, we etch 5 μm of diamond on each side of the substrate using Ar/Cl_2[30] and O_2 plasma[31−33] as a stress-relief etch to eliminate the residual polishing damage (see Supporting Information). A laser-cut quartz shadow mask is then used to mask the diamond for another 20 or 30 μm deep etch on one side of the sample (etch rate 5 μm/h). After lifting the quartz mask, we end up with a 10 or 20 μm diamond membrane suspended in a 40 μm frame. Atomic force microscopy (AFM) shows a surface roughness of <0.3 nm. A focused gallium ion beam (FIB, 30 kV, 20 nA) is used to mill the parabolic SIL structure on the diamond membrane. After FIB milling, the diamond surface is substantially graphitized and contains implanted gallium atoms (20 nm in depth).[34] We then etch away the top 100 nm of damaged diamond using Ar/Cl_2 plasma, followed by a 120 nm O_2 plasma etch to oxygen terminate the diamond surface. A boiling triacid bath

DOI: 10.1021/acs.nanolett.9b02430
Nano Lett. 2019, 19, 7021−7027

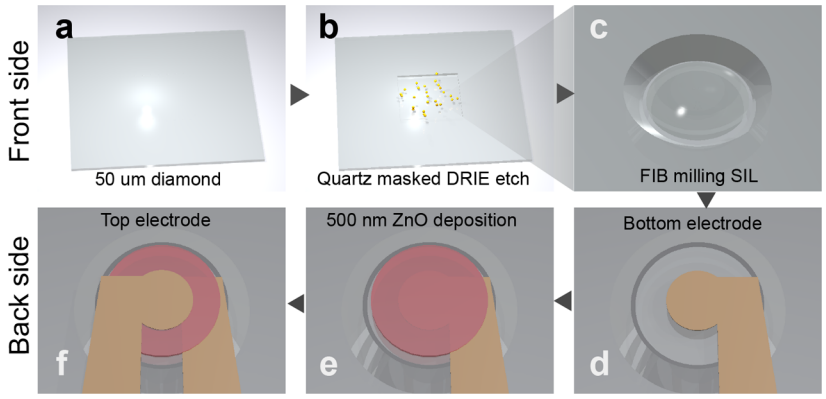

Figure 2. Fabrication process flow of the device starting from (a) a 50 μm thick double-side-polished diamond plate; (b) Deep reactive-ion etching (DRIE) etch of a diamond membrane down to 20 or 10 μm using Ar/Cl_2 and O_2 plasma, using a laser cut quartz mask; (c) mill the parabolic SIL using focused Ga ion beam. Postmilling plasma cleaning removes Ga damage and graphitization of substrate surface. (d–f) A ZnO piezoelectric transducer is fabricated on the backside of the SIL.

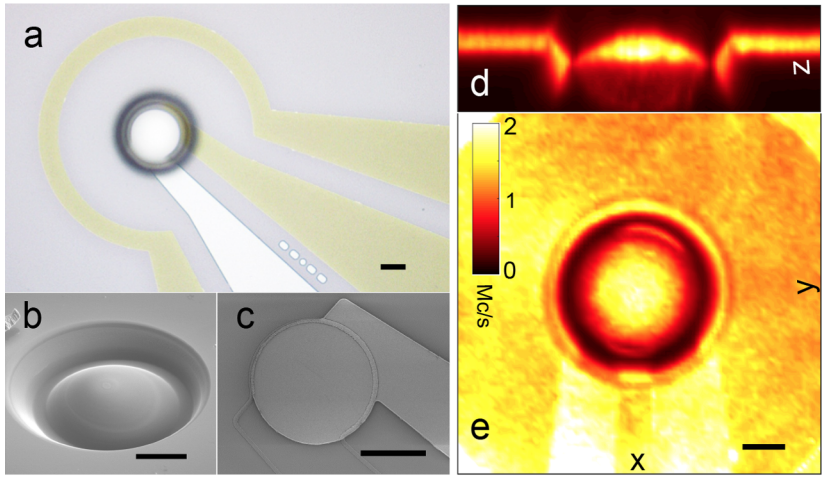

Figure 3. Micrographs and photoluminescence images of the finished device on an optical grade diamond substrate. (a) Device viewed from SIL side. Encircling the device is a microwave antenna used for magnetic resonance control of the spins inside the mechanical resonator. (b) SEM image of the milled solid immersion lens (radius of curvature 20 μm). (c) SEM image of the transducer on the backside of the SIL. (d,e) Photoluminescence image in a cross section view and a front view of the device (10 μm thick), collected using a home-built confocal microscope. There is enhancement in fluorescence collection of the NV ensemble in the SCHBAR owing to the integrated SIL. The scale bars in all figures are 10 μm in length.

containing equal parts of sulfuric, nitric, and perchloric acid is used to further clean off any residual contamination on the diamond. Optical profilometry and laser-scanning confocal microscopy have been used to confirm the profile accuracy of the SIL. The diamond membrane is then flipped with the planar side facing up. A piezoelectric zinc oxide (ZnO) transducer, consisting of bottom electrode (10 nm/90 nm Ti/Pt), 500 nm ZnO, top electrode (10 nm/180 nm Ti/Pt), and a microwave antenna are then lithographically defined and sputtered to finish the device fabrication.

Figure 3a–c shows the images of a finished diamond device. We measure the photoluminescence (PL) of the NV center ensemble inside the diamond SCHBAR using a home-built confocal microscope, where a 532 nm laser is used for excitation and a 630 nm long pass filter is used for PL collection in the phonon sideband emission of NV centers. Figure 3d,e shows the cross section and the front PL scan of a 10 μm device at an incident laser power of 150 μW. There is a clear enhancement of PL collection inside the resonator. This, in combination with the spin measurement reported later in the Letter, confirms that the NV centers are intact after fabrication.

The device is then wire-bonded to a circuit board for electrical measurement. A vector network analyzer (VNA) is used to characterize the scattering parameter (S-parameter) of the device. When the resonator is driven on the resonance, the microwave power is dissipated in the resonator and converted into mechanical energy, launching acoustic waves and enabling the resonance to be detected as a decrease in the reflected microwave power. The electromechanical response of the device is well described by the modified Butterworth Van-Dyke model,[35] and the mechanical quality factor, Q, can be extracted from the VNA measurements. After mounting the devices in vacuum on a coldfinger of a helium-flow cryostat, we perform electrical measurements as a function of temperature. The results are shown in Figure 4. The frequency and quality factor product is $f \times Q > 10^{12}$ for a 20 μm thick diamond device at room temperature and $f \times Q > 10^{13}$ for a 20 μm thick SiC device at low temperature. For the SiC device, we change the order of fabrication to enable a test of the Q-enhancement due to the curved acoustic mirror. In this case, we mill the SIL after

DOI: 10.1021/acs.nanolett.9b02430
Nano Lett. 2019, 19, 7021–7027

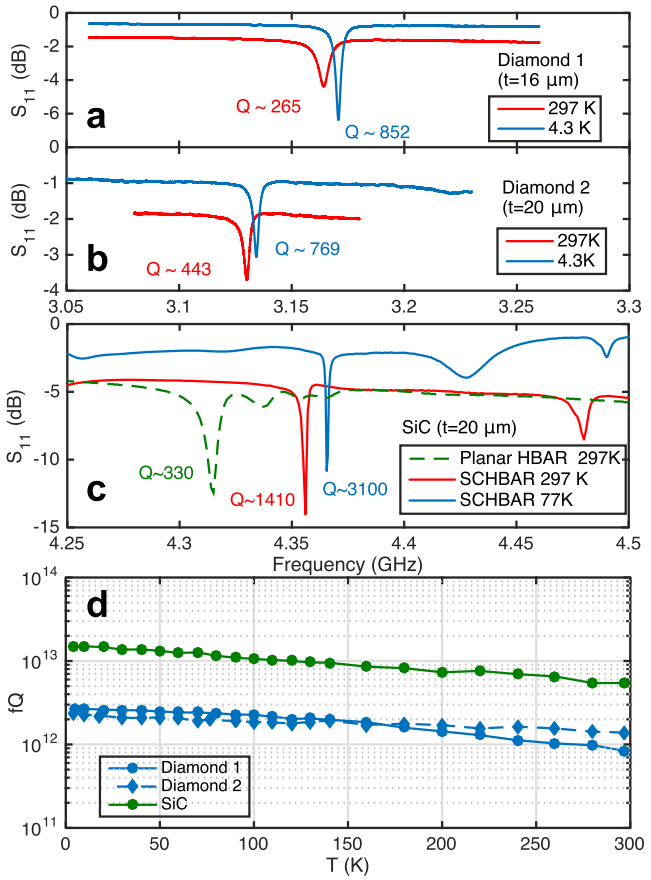

Figure 4. (a−c) S-parameters characterization of the device using a vector network analyzer. Similar fabrication has been done for both (a,b) diamond and (c) 4H-SiC substrate. For the SiC device, the SIL is milled after the fabrication of transducer. Compared to a planar HBAR structure (green dashed line), the incorporation of a SIL increases the quality factor by more than three times. (d) Quality factors are extracted from the measured S-parameters as a function of temperature.

the piezoelectric transducer fabrication, enabling a separate measurement of both a planar and a semiconfocal version of the same device. We find a >3× improvement in the quality factor with the addition of the SIL. We have also found similar effects in 10 μm thick diamond devices (see Supporting Information), indicating that the additional acoustic confinement adds in the suppression of acoustic diffraction loss. Theoretically,[36−41] the quality factor of the current diamond device is limited by phonon scattering, $f \times Q = 3-4 \times 10^{13}$ at room temperature (see Supporting Information), which is an order of magnitude higher than the measured value. Possible sources for the extra damping can be surface dissipation and material losses within the piezoelectric transducer, which are not included in our estimate.

Next we characterize the defect spins in the resonator and their coupling to the phonon mode. Although we detected silicon vacancy (V_{Si}) center emission in the SiC device (see Supporting Information), indicating the possibility of acoustic control of defect system in SiC, here we focus on NV center spin measurements using a diamond SCHBAR.

At room temperature, both the ground and the excited states of an NV center are spin triplets. The ground-state electron spin $|\pm1\rangle$ state degeneracy can be lifted via their coupling to magnetic and strain fields (Figure 4a), depicted by the Hamiltonian[2]

$$H_{NV} = (D_0 + d_{\parallel}\epsilon_z)S_z^2 + \gamma_{NV}\vec{B}\cdot\vec{S} + d_{\perp}[\epsilon_y(S_xS_y + S_yS_x) - \epsilon_x(S_x^2 - S_y^2)] \quad (1)$$

where $D_0 = (2\pi)2.87$ GHz is the zero-field splitting, $\gamma_{NV} = (2\pi)2.8$ MHz/G is the gyromagnetic ratio, $\vec{S}$ is the electron spin of an NV center ($S = 1$), $d_{\perp}(d_{\parallel})$ is the spin coupling strength to the transverse (longitudinal) strain field $\epsilon_{\perp}(\epsilon_{\parallel})$. Three sets of qubits can therefore be formed: magnetically driven single quantum spin transitions between $\{|0\rangle,|-1\rangle\}$ and $\{|0\rangle,|+1\rangle\}$ states and the mechanically driven double quantum spin transition between $\{|+1\rangle,|-1\rangle\}$ states.[7] We use the latter one to quantitatively characterize the resonator performance and to study the efficiency of defect spin coupling to the resonator mode in a diamond SCHBAR device.

All measurements are made at room temperature using a 20 μm thick diamond SCHBAR. We first apply an external magnetic field of 558.6 G, axially aligned to the N−V axis. This splits the $|+1\rangle$ and $|-1\rangle$ ground spin states of the NV center ensemble due to the Zeeman effect (Figure 4a). At 558.6 G, the spin $|+1\rangle$ and $|-1\rangle$ state separation is in resonance with the phonon mode frequency, ω_m. We then launch acoustic waves in the resonator by applying microwave power to the transducer at the resonator frequency 3.13 GHz. Coherent spin transitions can thus be induced by the acoustic wave through the transverse spin-strain coupling.[7,42]

Note that the operating magnetic field strength is close to the excited-state level anticrossing (ELAC) at 508 G.[43] By optical pumping in a well-aligned magnetic field, we can induce a strong polarization of the $I = 1$ nuclear spin of ^{14}N into its $|m_I = +1\rangle$ state (Figure 4b). By working with only a single hyperfine state, we greatly improve the signal-to-noise ratio and reduce the complexity of the system dynamics.

Now we test the mechanical driving efficiency and coherence. To pinpoint the mechanically driven spin resonance, we perform optically detected mechanical spin resonance (ODMSR) measurements as described in ref 7 (see Supporting Information). We observe a single resonance peak in the spectrum, confirming the strong nuclear spin polarization within the NV center ensemble. We then perform mechanically driven Rabi measurements of the $|+1\rangle$ and $|-1\rangle$ states as a function of microwave power applied to the transducer. We observe high contrast Rabi oscillations at a rate $(2\pi)2.19(14)$ MHz/V_p, where V_p is the peak voltage applied to the input port of our device. Transverse NV center spin-strain coupling, $d_{\perp}$, has been previously measured at around 20 GHz/strain,[12,44] enabling us to estimate that the current device has a high power-to-strain efficiency of $1.59(14) \times 10^{-4}$ V_p^{-1} (see Supporting Information). This value is reasonable relative to the COMSOL simulation result and consistent with the measured quality factor being lower than COMSOL would predict. We note that the simulation uses empirical values of structural and dielectric loss and does not consider all dissipation sources. Compared to an HBAR device,[42] the power-to-strain efficiency has improved by 60−160 times. Lastly, we measure the spin coherence within the mechanically controlled $\{|+1\rangle, |-1\rangle\}$ subspace and within the magnetically controlled $\{|0\rangle, |-1\rangle\}$ subspace (Figure 5e). We find T_2^* is 610(110) ns and 840(120) ns, respectively.

With the demonstrated voltage-to-strain transduction, the diamond SCHBAR device has roughly the same efficiency for spin-strain driving as the microwave antenna has for magnetic

DOI: 10.1021/acs.nanolett.9b02430
Nano Lett. 2019, 19, 7021−7027

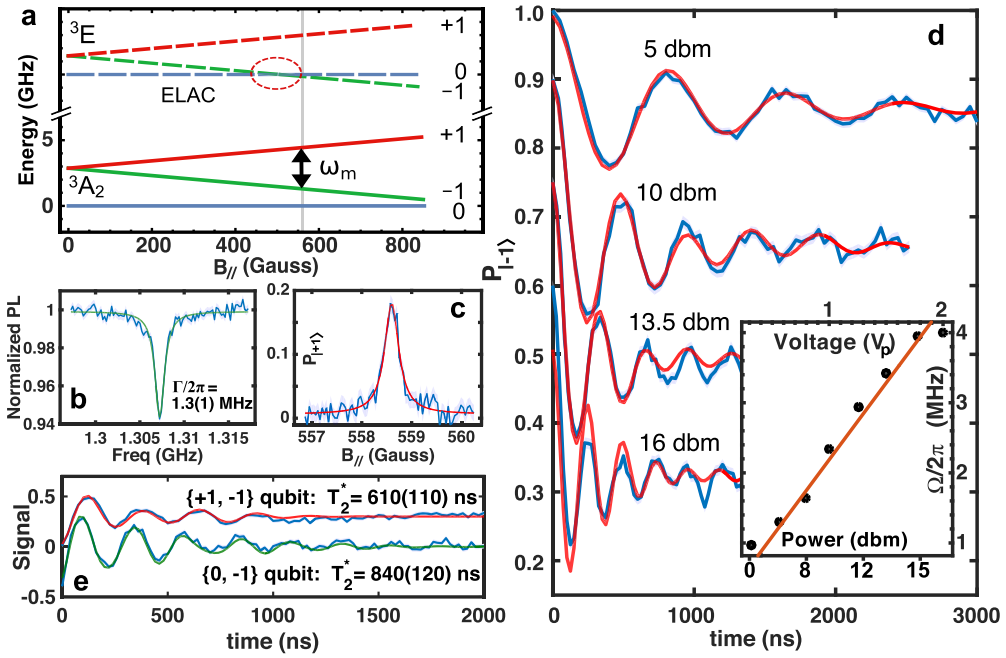

Figure 5. (a) Energy level diagram of an NV center at room temperature. The targeted 3.13 GHz phonon mode is in resonance with the $\{|+1\rangle, |-1\rangle\}$ transition at magnetic fields around 558.6 G, close to the ELAC. (b) Optically detected magnetic resonance (ODMR) spectrum for the $\{|0\rangle, |-1\rangle\}$ transition reveals strong nuclear spin polarization of the NV ensemble. (c) ODMSR measurement also shows a single hyperfine peak which is in agreement with (b). (d) Rabi oscillations between the $\{|+1\rangle, |-1\rangle\}$ states of the NV center ensemble induced by acoustic wave driving at 3.13 GHz taken at various driving powers. The inset is a linear fit to the Rabi frequency dependence on applied MW power to the transducer, giving a slope of $(2\pi)2.19(14)$ MHz/V_p. (e) Ramsey measurement of the $\{|0\rangle, |-1\rangle\}$ qubit state using magnetic driving, and $\{|+1\rangle, |-1\rangle\}$ qubit state using mechanical wave driving.

driving (note that the antenna in the current device has a radius of 50 μm, which is optimized to reduce field gradient for ensemble spin control). This is promising for using mechanical driving as an added resource, for example, strong mechanical driving of NV center spins can be used to extend the coherence time via continuous dynamical decoupling.[10,11] Additionally, the ability to perform pulsed spin control protocols within the $\{|+1\rangle, |-1\rangle\}$ subspace, which are enabled by sizable Rabi frequencies and ~40 ns ring-up/down times, makes quantum control a strong application of our device. These capabilities will be a useful resource for magnetic sensing in the double-quantum basis[45] and for nonmagnetic sensing modalities.

Apart from fast mechanical control of defect spins, a SCHBAR operates at a high enough frequency to be cooled to its mechanical ground state using a dilution refrigerator (~100 mK). The single spin-phonon cooperativity of the current device is low, even at low temperature (T = 100 mK), $C = \frac{g^2 T_2}{\kappa \bar{n}} \sim 10^{-8}$, where $g \sim 1$ Hz is the single spin-phonon coupling rate calculated from the zero-point motion of resonator (note that this is 10^3 higher than HBAR devices made in the past[7]), $T_2 \sim 10$ ms is the coherence time of an NV center spin, $\kappa = \omega_m/Q$ is the resonator damping rate and $\bar{n}$ is the phonon occupation number at temperature T. The ensemble spin-phonon coupling is enhanced relative to the single spin-phonon coupling by $\sim\sqrt{N}$, where N is the number of coupled NV centers. For a dense ensemble[46] of NV centers with density 10^{19} cm^{-3}, there are close to $N = 10^{10}$ addressable NV centers in a $(10\,\mu\text{m})^3$ resonator. The maximum spin-phonon coupling is then $\sqrt{N}g \sim 100$ kHz. However, inhomogeneity induced ensemble spectral broadening (~MHz) can degrade the effective coupling[47] and we expect the collective cooperativity will be $\sim 10^{-3}$. To further increase the coupling, defect centers with stronger intrinsic spin-phonon coupling can be considered, that is, SiV centers in diamond have been shown to have defect spin−strain coupling of ~100 THz/strain,[48] around 5000 times larger than that for an NV center. In this case, however, the potential spectral inhomogeneity in the ensemble spin transition requires further investigation to understand if it is practical for resonator coupling. If we can find operating parameters that minimize strain-induced inhomogeneity of the spin transition frequency without limiting the spin-strain coupling strength, then SiV center ensembles could be a good candidate system for hybrid spin-mechanical systems. For example, if we assume a moderate inhomogeneous spectral broadening that is typical for NV centers in the high-field limit, a SiV center ensemble with a density of only 10^{16} cm^{-3} could enter the strong ensemble-resonator coupling regime.

Improvements to the device quality factors and power handling are possible by replacing ZnO with high quality AlN which has higher resistivity, or by using superconducting electrodes that can help to mitigate the electron−phonon dissipation in the metal electrodes. Further enhancement in single spin-phonon coupling can be obtained by reduction of the device volume, however, such down-scaling must be accompanied by a shift to a higher resonator frequency or alteration of the SIL geometry to explicitly account for wavefront geometry to maintain a high Q.

In conclusion, we report the design, fabrication, and testing of a diamond (SiC) SCHBAR device. SCHBAR marks the first step toward a microscale BAW resonator device. We obtain $f \times Q > 10^{12}(10^{13})$ for a diamond (SiC) SCHBAR and demonstrate efficient and high-rate phonon-induced NV center

DOI: 10.1021/acs.nanolett.9b02430
Nano Lett. 2019, 19, 7021−7027

Rabi oscillations at $(2\pi)2.19(14)$ MHz/V_p. The device enables direct circuit integration and it is ideal for fast mechanical control of defect spins. Further integration of a dense spin ensemble along with improvements in the device quality factor could enable study of defect spin-phonon interaction at the quantum level.

■ ASSOCIATED CONTENT

Supporting Information

The Supporting Information is available free of charge on the ACS Publications website at DOI: 10.1021/acs.nanolett.9b02430.

Simulation results; device optical performance analysis; detailed fabrication parameters; device quality factor analysis; device dimension scaling; experimental pulse sequence and strain evaluation (PDF)

■ AUTHOR INFORMATION

Corresponding Author

*E-mail: gdf9@cornell.edu.

ORCID

Gregory D. Fuchs: 0000-0003-4343-8523

Notes

The authors declare no competing financial interest.

■ ACKNOWLEDGMENTS

Research support was provided by the Office of Naval Research (Grant N000141712290) and by the DARPA DRINQS program (Cooperative Agreement #D18AC00024). Any opinions, findings, and conclusions or recommendations expressed in this publication are those of the author(s) and do not necessarily reflect the views of DARPA. R.S.D. acknowledges support of the Air Force Office of Scientific Research Hybrid Materials MURI under award number FA9550-18-1-0480. Device fabrication was performed in part at the Cornell NanoScale Science and Technology Facility, a member of the National Nanotechnology Coordinated Infrastructure, which is supported by the National Science Foundation (Grant ECCS-15420819), and at the Cornell Center for Materials Research Shared Facilities which are supported through the NSF MRSEC program (Grant DMR-1719875).

■ REFERENCES

(1) Awschalom, D. D.; Hanson, R.; Wrachtrup, J.; Zhou, B. B. *Nat. Photonics* **2018**, *12*, 516.

(2) Doherty, M. W.; Manson, N. B.; Delaney, P.; Jelezko, F.; Wrachtrup, J.; Hollenberg, L. C. *Phys. Rep.* **2013**, *528*, 1−45.

(3) Sukachev, D. D.; Sipahigil, A.; Nguyen, C. T.; Bhaskar, M. K.; Evans, R. E.; Jelezko, F.; Lukin, M. D. *Phys. Rev. Lett.* **2017**, *119*, 223602.

(4) Christle, D. J.; Falk, A. L.; Andrich, P.; Klimov, P. V.; Hassan, J. U.; Son, N. T.; Janzén, E.; Ohshima, T.; Awschalom, D. D. *Nat. Mater.* **2015**, *14*, 160.

(5) Widmann, M.; Lee, S.-Y.; Rendler, T.; Son, N. T.; Fedder, H.; Paik, S.; Yang, L.-P.; Zhao, N.; Yang, S.; Booker, I.; et al. *Nat. Mater.* **2015**, *14*, 164.

(6) Barson, M. S.; Peddibhotla, P.; Ovartchaiyapong, P.; Ganesan, K.; Taylor, R. L.; Gebert, M.; Mielens, Z.; Koslowski, B.; Simpson, D. A.; McGuinness, L. P.; et al. *Nano Lett.* **2017**, *17*, 1496−1503.

(7) MacQuarrie, E. R.; Gosavi, T. A.; Jungwirth, N. R.; Bhave, S. A.; Fuchs, G. D. *Phys. Rev. Lett.* **2013**, *111*, 227602.

(8) Bernien, H.; Hensen, B.; Pfaff, W.; Koolstra, G.; Blok, M.; Robledo, L.; Taminiau, T.; Markham, M.; Twitchen, D.; Childress, L.; et al. *Nature* **2013**, *497*, 86.

(9) Kalb, N.; Reiserer, A. A.; Humphreys, P. C.; Bakermans, J. J.; Kamerling, S. J.; Nickerson, N. H.; Benjamin, S. C.; Twitchen, D. J.; Markham, M.; Hanson, R. *Science* **2017**, *356*, 928−932.

(10) MacQuarrie, E. R.; Gosavi, T. A.; Bhave, S. A.; Fuchs, G. D. *Phys. Rev. B: Condens. Matter Mater. Phys.* **2015**, *92*, 224419.

(11) Barfuss, A.; Teissier, J.; Neu, E.; Nunnenkamp, A.; Maletinsky, P. *Nat. Phys.* **2015**, *11*, 820.

(12) Ovartchaiyapong, P.; Lee, K. W.; Myers, B. A.; Jayich, A. C. B. *Nat. Commun.* **2014**, *5*, 4429.

(13) Burek, M. J.; Cohen, J. D.; Meenehan, S. M.; El-Sawah, N.; Chia, C.; Ruelle, T.; Meesala, S.; Rochman, J.; Atikian, H. A.; Markham, M.; et al. *Optica* **2016**, *3*, 1404−1411.

(14) Cady, J.; Michel, O.; Lee, K.; Patel, R.; Sarabalis, C. J.; Safavi-Naeini, A. H.; Jayich, A. B. *Quantum Science and Technology* **2019**, *4*, 024009.

(15) Golter, D. A.; Oo, T.; Amezcua, M.; Stewart, K. A.; Wang, H. *Phys. Rev. Lett.* **2016**, *116*, 143602.

(16) Chen, H. Y.; MacQuarrie, E. R.; Fuchs, G. D. *Phys. Rev. Lett.* **2018**, *120*, 167401.

(17) Whiteley, S. J.; Wolfowicz, G.; Anderson, C. P.; Bourassa, A.; Ma, H.; Ye, M.; Koolstra, G.; Satzinger, K. J.; Holt, M. V.; Heremans, F. J.; et al. *Nat. Phys.* **2019**, *15*, 490−495.

(18) O'Connell, A. D.; Hofheinz, M.; Ansmann, M.; Bialczak, R. C.; Lenander, M.; Lucero, E.; Neeley, M.; Sank, D.; Wang, H.; Weides, M.; et al. *Nature* **2010**, *464*, 697.

(19) Chu, Y.; Kharel, P.; Renninger, W. H.; Burkhart, L. D.; Frunzio, L.; Rakich, P. T.; Schoelkopf, R. J. *Science* **2017**, *358*, 199−202.

(20) Aigner, R. *SAW and BAW technologies for RF filter applications: A review of the relative strengths and weaknesses*; IEEE Ultrasonics Symposium, Beijing China; IEEE: 2008; pp 582−589; DOI: 10.1109/ULTSYM.2008.0140.

(21) Fang, S. R.; Zhang, S.; Lu, Z. F. *IEEE transactions on ultrasonics, ferroelectrics, and frequency control* **1989**, *36*, 178−184.

(22) Shilton, R.; Tan, M. K.; Yeo, L. Y.; Friend, J. R. *J. Appl. Phys.* **2008**, *104*, 014910.

(23) Galliou, S.; Goryachev, M.; Bourquin, R.; Abbé, P.; Aubry, J. P.; Tobar, M. E. *Sci. Rep.* **2013**, *3*, 2132.

(24) Kharel, P.; Chu, Y.; Power, M.; Renninger, W. H.; Schoelkopf, R. J.; Rakich, P. T. *APL Photonics* **2018**, *3*, 066101.

(25) Bhugra, H.; Piazza, G. *Piezoelectric MEMS resonators*; Springer, 2017.

(26) Baron, T.; Lebrasseur, E.; Bassignot, F.; Martin, G.; Pétrini, V.; Ballandras, S. *Modeling and Measurement Methods for Acoustic Waves and for Acoustic Microdevices*; InTechOpen, 2013.

(27) Siegman, A. *Lasers*; Oxford University Press, 1986.

(28) Hadden, J.; Harrison, J.; Stanley-Clarke, A.; Marseglia, L.; Ho, Y.-L.; Patton, B.; O'Brien, J.; Rarity, J. *Appl. Phys. Lett.* **2010**, *97*, 241901.

(29) Yu, P.-L.; Opondo, N.; Dai, S.; Jiang, B.; Morisette, D. T.; Bhave, S. A. *Single Crystalline 4H-SiC Membrane Resonators*. IEEE International Frequency Control Symposium (IFCS), Olympic Valley, CA, USA; IEEE: 2018; pp 1−5; DOI: 10.1109/FCS.2018.8597489.

(30) Lee, C.; Gu, E.; Dawson, M.; Friel, I.; Scarsbrook, G. *Diamond Relat. Mater.* **2008**, *17*, 1292−1296.

(31) Friel, I.; Clewes, S. L.; Dhillon, H. K.; Perkins, N.; Twitchen, D. J.; Scarsbrook, G. A. *Diamond Relat. Mater.* **2009**, *18*, 808−815.

(32) Appel, P.; Neu, E.; Ganzhorn, M.; Barfuss, A.; Batzer, M.; Gratz, M.; Tschöpe, A.; Maletinsky, P. *Rev. Sci. Instrum.* **2016**, *87*, 063703.

(33) Ruf, M.; IJspeert, M.; van Dam, S.; de Jong, N.; van den Berg, H.; Evers, G.; Hanson, R. *Nano Lett.* **2019**, *19*, 3987.

(34) Bayn, I.; Bolker, A.; Cytermann, C.; Meyler, B.; Richter, V.; Salzman, J.; Kalish, R. *Appl. Phys. Lett.* **2011**, *99*, 183109.

(35) Larson, J. D.; Bradley, P. D.; Wartenberg, S.; Ruby, R. C. Modified Butterworth-Van Dyke circuit for FBAR resonators and

DOI: 10.1021/acs.nanolett.9b02430
Nano Lett. 2019, 19, 7021−7027

automated measurement system. 2000 IEEE Ultrasonics Symposium. Proceedings. An International Symposium (Cat. No. 00CH37121), San Juan, Puerto Rica, USA; IEEE: 2000; pp 863−868; DOI: 10.1109/ULTSYM.2000.922679.
(36) Zener, C. *Phys. Rev.* **1937**, *52*, 230.
(37) Landau, L.; Rumer, G. *Phys. Z. Sowjetunion* **1937**, 11.
(38) Akhieser, A. *J. Phys.(Ussr)* **1939**, *1*, 277.
(39) Woodruff, T.; Ehrenreich, H. *Phys. Rev.* **1961**, *123*, 1553.
(40) Landau, L. D. *Theory of elasticity*; Elsevier, 1986.
(41) Lifshitz, R.; Roukes, M. L. *Phys. Rev. B: Condens. Matter Mater. Phys.* **2000**, *61*, 5600.
(42) MacQuarrie, E. R.; Gosavi, T. A.; Moehle, A. M.; Jungwirth, N. R.; Bhave, S. A.; Fuchs, G. D. *Optica* **2015**, *2*, 233−238.
(43) Jacques, V.; Neumann, P.; Beck, J.; Markham, M.; Twitchen, D.; Meijer, J.; Kaiser, F.; Balasubramanian, G.; Jelezko, F.; Wrachtrup, J. *Phys. Rev. Lett.* **2009**, *102*, 057403.
(44) Teissier, J.; Barfuss, A.; Appel, P.; Neu, E.; Maletinsky, P. *Phys. Rev. Lett.* **2014**, *113*, 020503.
(45) Taylor, J. M.; Cappellaro, P.; Childress, L.; Jiang, L.; Budker, D.; Hemmer, P. R.; Yacoby, A.; Walsworth, R.; Lukin, M. *Nat. Phys.* **2008**, *4*, 810.
(46) Choi, J.; Choi, S.; Kucsko, G.; Maurer, P. C.; Shields, B. J.; Sumiya, H.; Onoda, S.; Isoya, J.; Demler, E.; Jelezko, F.; et al. *Phys. Rev. Lett.* **2017**, *118*, 093601.
(47) Kubo, Y.; Ong, F.; Bertet, P.; Vion, D.; Jacques, V.; Zheng, D.; Dréau, A.; Roch, J.-F.; Auffèves, A.; Jelezko, F.; et al. *Phys. Rev. Lett.* **2010**, *105*, 140502.
(48) Meesala, S.; Sohn, Y.-I.; Pingault, B.; Shao, L.; Atikian, H. A.; Holzgrafe, J.; Gündoğan, M.; Stavrakas, C.; Sipahigil, A.; Chia, C.; et al. *Phys. Rev. B: Condens. Matter Mater. Phys.* **2018**, *97*, 205444.

DOI: 10.1021/acs.nanolett.9b02430
Nano Lett. 2019, 19, 7021−7027